



Study on hydrodynamic characteristics and backwashing efficiency of three types turbines of axial dynamic backwashing technology for oilfield wastewater filter

Zhen Wei^{a,b}, YanXin Yu^{a,b}, YuJun Yi^{a,b}, ZhongChen Yu^{c,*}, JunFeng Li^d, QiuGang Wang^d

^aSchool of Environment, Beijing Normal University, Beijing 100875, China, emails: wz_water@sina.com (Z. Wei), 1836185557@qq.com (Y. Yu), yiyujun@bnu.edu.cn (Y. Yi)

^bState Key Laboratory of Water Environment Simulation and Pollution Control, Beijing Normal University, Beijing 100875, China

^cSchool of Civil and Architectural Engineering, Northeast Petroleum University, Daqing 163318, Heilongjiang, China, Tel. +0086-182 4588 2000; email: 909681949@qq.com

^dSchool of Water Conservancy and Architecture Engineering, Shihezi University, Shihezi 832000, Xinjiang, China, emails: ljfshz@126.com (J. Li), 782823974@qq.com (Q. Wang)

Received 10 May 2020; Accepted 16 December 2020

ABSTRACT

Walnut shell media plays an important role in polymer flooding and alkaline-surfactant-polymer oil recovery wastewater treatment, but the regeneration of walnut shell has always been a difficult problem. To solve this problem, axial dynamic backwashing technology has shown good regenerative effects in practice, and investigation on the hydrodynamic characteristics and backwashing efficiency of axial turbine filtration used for the filtration are necessary. In this study, three types of turbines (flatness, twisted, and airfoil loading) were experimentally studied and compared in terms of their backwashing performances. The cascade efficiency was calculated and it was concluded that airfoil loading was the key to improve cascade efficiency. The flow field distributions of three kinds of the turbine were analyzed, and the results showed that the flatness and twisted characteristics determined the flow field distribution forms. The vortex energy loss efficiency was calculated and the results showed that the flow field distribution determined the vortex energy loss. The G value of three kinds of turbine backwashing showed that the G value of axial dynamic backwashing technology was larger and more controllable than that of gas–water backwashing. The local backwashing G value could reach 35–45 times of the G value of gas–water backwashing at the optimal rotational speed of 1,420–1,810 rpm. The relationship between three geometric characteristics and backwashing efficiency was finally established—the head can be increased by loading airfoil, and the backwashing G value can be increased by changing the degree of blade distortion. This research not only provides technical support for the lower cost operation of axial dynamic backwashing technology but also will contribute to providing an important reference for other backwashing technologies by pump washing.

Keywords: Axial turbine; Hydrodynamic characteristics; Fluent; G value; Backwashing

* Corresponding author.

1. Introduction

Currently, most Chinese oilfields have been in their middle or later stage of development and the produced oil contains a very large volume of water. The oily water produced after the main separation of produced oil is called produced water. In order to avoid produced water damage to the environment, it is the easiest and the most economical way to treat the produced water for reinjection [1]. According to the reinjection standards (SY/T 5329-94), the concentration of oil should be controlled for injection back [2]. However, the application of enhanced oil recovery (EOR) technology complicates the composition of produced water [3]. Especially, the alkaline-surfactant-polymer (ASP) flooding technology, developed on the basis of polymer flooding oil recovery technology, makes the produced water not only contain a polymer, oil, suspended solids, but also include alkali, surfactant, and other substances [4–7]. Surfactants tend to decrease the oil/water interfacial tension; alkali saponifies indigenous acidic components in the crude mixture, resulting in higher water solubility and lower interfacial tension (IFT); and polymers increase the viscosity of the aqueous phase [8,9]. Thus, the produced water from ASP flooding forms a complex and stable emulsion system that oil droplets get more difficult to remove than that formed from water flooding [4]. Undoubtedly, this increases the difficulty of sewage treatment and put forward higher requirements for the treatment process.

Among the technologies applied, filtration is usually the last and most important step in oilfield wastewater treatment and is the crucial technology to control the concentration of oil and SS [1,10]. The filtration mainly depends on the interception and adsorption of the filtration medium. To date, various solid materials have been used as filter media, such as sand, anthracite, and walnut shell. With the application of EOR technology, as the walnut shell media have the unique physicochemical properties to effectively absorb the dispersed oil and other organic substance droplets, more walnut shell filters have been applied [10]. During the operation of the walnut shell filter, the filter media would be saturated when the pollution content of treated water or the total pressure drop of the filter bed reaches a certain value, and then a backwashing process is necessary. The backwashing process is the basis to ensure the normal operation of the walnut shell filter. The backwashing mechanisms of filter media include the hydraulic shearing between media particles and water and the collisions between media particles [11]. Both effects are measured in hydraulic gradient value (G). Currently, three backwashing modes have been proposed, including water backwash, the combined backwash of air and water, water backwash assisted by ultrasonic or mechanical stirring, all these three modes have been confirmed to be feasible [12–14]. As the combined backwash mode of air and water is more complex in system and consumes more energy, simple water backwashing, and water backwashing assisted by mechanical stirring backwashing modes are most widely used in the oilfields of China now [10].

The related parameters of water backwashing processes for the walnut shell are listed: the diameter is 0.5–1 mm, the density is 1,334 kg/m³, filter media bed height is

0.7–1 m, backwashing rate of water is 8–10 L/(m² s), initial pressure of backwash water is 0.03–0.08 MPa, and the pressure drop during backwashing process is about 20%.

However, as the G value produced by water backwashing is the smallest of the three methods, water backwashing cannot show good cleaning performance, especially when the viscosity of attached dirt increases due to polyacrylamide. The mechanical assisted backwashing method makes the filter material get a better cleaning effect by means of mechanical stirring. One way of this method makes the filter material violently roll in the filter to strengthen the backwashing effect. However, the tumbling filter material easily blocks the water outlet, resulting in backwashing flow smaller and poor walnut shell cleaning effect. Another external circulation way was proposed, in which dirty media are firstly transported by a slurry pump to a separated regenerator and the washing process is completed there, then those clean media are returned to the filter by the recycled slurry pump [10]. In addition, an innovative backwash method (the axial dynamic backwashing technique) was proposed, in which the dirty media are scrubbed by a cyclic inner flow field created by the rotation of the turbine [15,16]. On the one hand, the filter material is subjected to intense rubbing by the turbine. On the other hand, the swirling flow field created by the turbine enables the distribution of filter material and wastewater inside and outside under the action of density difference, achieving further separation and not blocking the inner water outlet. The technology has a good treatment effect for oil recovery wastewater from polymer flooding (ORWPF) and oil recovery wastewater from alkaline-surfactant-polymer flooding (ORWASPF) [17–20].

For the design of an efficient backwashing turbine, studies on backwashing process are important. However, the existing study on the axial dynamic backwashing technique mainly focused on the parameters of backwashing time and strength [21], the study concerning on the turbine, the core component of the technology, is rare, which hinders the further development of the technology. In this paper, three types of turbines (flat blade turbine, bent plate turbine, and airfoil turbine) were experimentally studied and compared in terms of their backwashing performances. Aim to (1) study the hydrodynamic performance by using the method of efficiency calculation and numerical simulation by fluent, (2) compare the relationship between geometric characteristics and backwashing efficiency which is established with G value as the standard and energy as the bridge. Meanwhile, those factors affecting the performance of mechanical stirring mode are further investigated. The study will contribute to providing the important reference for manufacturing high-efficiency backwashing turbine.

2. Methodology

2.1. Models of turbine flow field

The flat blade was a flat plate, and the internal and external directrix equations of the blade is shown in Eq. (1). The bent blade was generated by the movement of straight generatrix which was always orthogonal to the axis of the cylinder and 90° to the surface of the cylinder [22], and internal and external directrix equations of the blade are

shown in Eqs. (1) and (2), and the relationship of outlet angle between internal and external directrix is shown in Eq. (3). An airfoil turbine was constructed by loading the airfoil onto a bent plate turbine. The airfoil (named NACA4412) was selected to make the chord length coincide with the middle line of the bent blade cascade, the back of the airfoil was used as the liquid-facing surface, the leading edge was used as the inlet angle of the cascade, the trailing edge was used as the outlet angle, and equally spaced N cascades were loaded and connected to form the blade surface. As the outlet angle of the airfoil changes little after loading, we thought airfoils turbine had the same outlet angle with bent plate turbine:

$$z = j \tan \beta_1 \quad (1)$$

$$z = j \tan \beta_2 \quad (2)$$

$$\tan \beta_2 = \frac{r_1}{r_2} \tan \beta_1 \quad (3)$$

The geometric model was established according to the mathematical models of turbine surface: set three blades, $\beta_1 = 30^\circ$, $r_1 = 20$ mm, $r_2 = 49$ mm, and the height of hub is 30 mm. In specially, the method given in the literature [23] was used for airfoil coordinate transformation in the turbine structure. The three turbine models are shown in Fig. 1.

2.2. Axial dynamic backwashing filter

The test device of axial dynamic backwashing filter was made of plexiglass and stainless steel, which was mainly composed of an internal circulation device, three-phase asynchronous motor, and frequency converter. The upper motor powered the internal turbine. Its rated power was 0.18 kW, rated voltage was 380 V, and rated speed was 1,400 rpm. The internal circulator device included an axial turbine and separator, and its external structure size was $\Phi 100$ mm \times 500 mm. The outer wall size was $\Phi 400$ mm \times 700 mm.

After backwashing beginning, firstly the filter bed of the walnut shell became fluidized under the action of water flow. Then the rotating turbine drew the fluidized medium into the internal circulation device to complete the rubbing, the fallen impurities were washed out with the flow

of water, and the filter material was separated from the internal circulation and fell back to the filter bed under the action of centrifugal force. The experimental setup of backwashing is shown in Fig. 2.

2.3. Calculation method of cascade efficiency

Turbine efficiency was divided into cascade efficiency and vortex loss efficiency. According to the infinite cascade theory, the work done by a turbine on a fluid could be regarded as the work done by an infinite number of the infinitesimal cascade, and the cascade efficiency could be obtained by analyzing the force exerted on the cascades.

2.3.1. Circumferential speed correction

In order to calculate the cascade efficiency accurately, the circumferential speed was corrected by considering the slip velocity.

Referring to Stodola's theory, axial turbines also have axial vortices. The axial vortex is a forced vortex, and the angular velocity is ω [24]. Finally, the v_{u2} of the outlet of the flat plate turbine could be obtained at the radius r , as shown in Eq. (4):

$$v_{u2} = \begin{cases} r\omega - \frac{v}{\tan \beta_1} - \frac{1}{2} \frac{(2r - r_1 - r_2)^2 r_2}{r(r_2 - r_1)} \omega, r \in \left(\frac{r_1 + r_2}{2}, r_2 \right) \\ r\omega - \frac{v}{\tan \beta_1} + \frac{1}{2} \frac{(2r - r_1 - r_2)^2 r_1}{r(r_2 - r_1)} \omega, r \in \left(r_1, \frac{r_1 + r_2}{2} \right) \end{cases} \quad (4)$$

Similarly, the circular velocity of the outlet velocity of the bent plate turbine at different radii could also be obtained, as shown in Eq. (5):

$$v_{u2} = \begin{cases} r\omega - \frac{rv}{r_1 \tan \beta_1} - \frac{1}{2} \frac{(2r - r_1 - r_2)^2 r_2}{r(r_2 - r_1)} \omega, r \in \left(\frac{r_1 + r_2}{2}, r_2 \right) \\ r\omega - \frac{rv}{r_1 \tan \beta_1} + \frac{1}{2} \frac{(2r - r_1 - r_2)^2 r_1}{r(r_2 - r_1)} \omega, r \in \left(r_1, \frac{r_1 + r_2}{2} \right) \end{cases} \quad (5)$$

The outlet of the airfoil turbine was affected by the same axial vortex, so v_{u2} was consistent with the bent plate turbine.

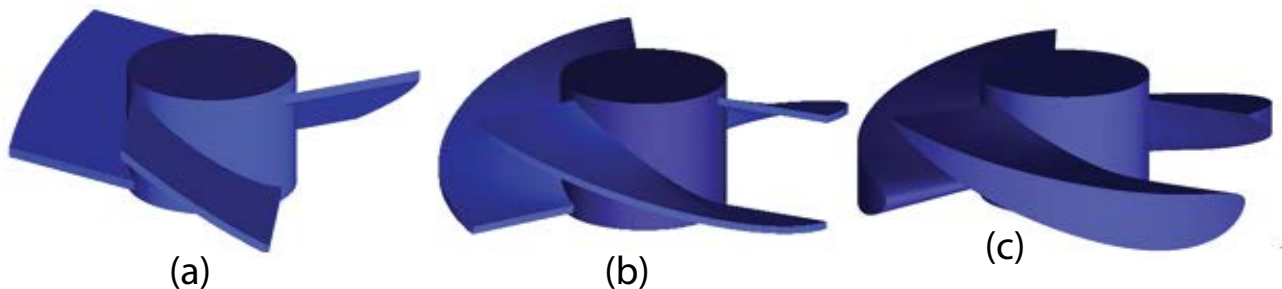


Fig. 1. Turbine model diagram, from left to right, flat turbine, bent plate turbine, and airfoil turbine.

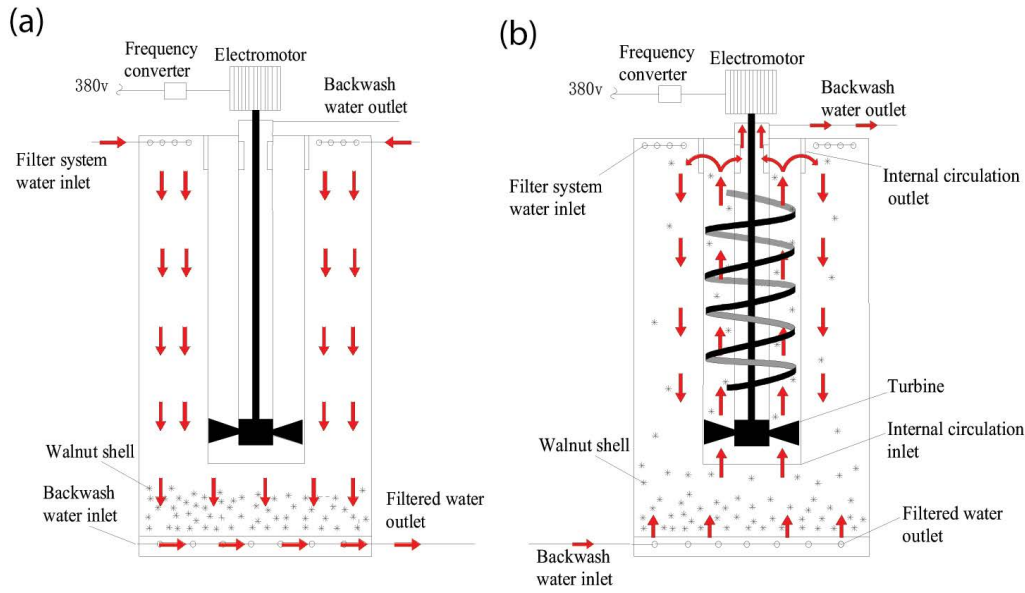


Fig. 2. Working process diagram of axial dynamic backwashing device: (a) filtration and (b) backwashing.

2.3.2. Calculation of cascade efficiency

The energy loss of the infinitesimal fluid was caused by the cascade resistance. By analyzing the cascade resistance, the cascade efficiency of flat and bent plate turbines were solved. Because the cascade flat and bent plate turbines were flat, according to the airfoil theory, the efficiency of the infinitesimal cascade was calculated according to Eq. (6):

$$\eta_p = 1 - \left(\frac{w_\infty}{u} \right) \frac{\sin \lambda}{\sin(\beta_\infty + \lambda)} \tag{6}$$

$$w_\infty = \sqrt{v^2 + \left(u - \frac{v_{u2}}{2} \right)^2} \tag{7}$$

The turbine cascade efficiency was obtained by integrating the infinitesimal cascade, as shown in Eq (8):

$$\eta_h = \frac{\int_{r_1}^{r_2} \eta_p 2\pi r v dr}{Q} \tag{8}$$

The difference between the calculation of cascade efficiency of airfoil turbine and bent plate turbine was the value of λ , and λ could be obtained from the lift-drag coefficient curve of airfoil. When the rotation speed was between 600 and 2,000 rpm, the Reynolds number was between 1.5×10^5 and 2×10^5 , and NACA4412 C_x and C_y could be obtained. Plugged C_x and C_y in Eq. (9) to get λ , used Eq. (6) to get η_p , and integrated to get η_h . In the calculation process, the efficiency of turbine cascade η_p was obtained by using the function fitting method.

$$\tan \lambda = \frac{F_x}{F_y} = \frac{C_x}{C_y} \tag{9}$$

2.4. Numerical models and simulation

2.4.1. Governing equations

The governing equations for the turbulent incompressible flow encountered in this research were the steady-state RANS equations for the conservation of mass and momentum, given as:

$$\frac{\partial \bar{p}}{\partial t} + \frac{\partial (\bar{\rho} \mu_i)}{\partial x_i} = 0 \tag{10}$$

$$\frac{\partial}{\partial t} (\bar{\rho} \mu_i) + \frac{\partial}{\partial x_j} (\bar{\rho} \mu_i \mu_j) = \rho F_i - \frac{\partial \bar{p}}{\partial x_i} + \frac{\partial}{\partial x_j} \left[\psi \left(\frac{\partial \bar{\mu}_i}{\partial x_j} + \frac{\partial \bar{\mu}_j}{\partial x_i} \right) \right] \tag{11}$$

To correctly account for turbulence, the Reynolds stresses were modeled in order to achieve the closure of Eq. (11). The modeling was based on the Boussinesq hypothesis to relate the Reynolds stresses to the mean velocity gradients within the flow. The Reynolds stresses are given by:

$$-\bar{\rho} \mu'_i \mu'_j = \psi_t \left(\frac{\partial \bar{\mu}_i}{\partial x_j} + \frac{\partial \bar{\mu}_j}{\partial x_i} \right) - \frac{2}{3} \delta_{ij} \cdot \left(\rho k + \psi_t \frac{\partial \bar{\mu}_i}{\partial x_i} \right) \tag{12}$$

For two-equation turbulence models, such as the $k-\epsilon$ variants, the turbulent viscosity was computed through the solution of two additional transport equations for the turbulent kinetic energy, k , and the turbulence dissipation rate, ϵ .

2.4.2. RNG $k-\epsilon$ turbulence model

To model the effective viscosity, the RNG $k-\epsilon$ turbulence model was used. The RNG model provided an option

to account for the effects of swirl or rotation by modifying the turbulent viscosity appropriately. RNG k - ε model was widely used in the flow field simulation of turbomachinery, such as pump [25–27].

The turbulence kinetic energy, k , and its rate of dissipation, ε , were obtained from the following transport equations:

$$\frac{\partial(\rho k \bar{\mu}_i)}{\partial x_i} = \frac{\partial}{\partial x_j} \left(\alpha_k \Psi_{\text{eff}} \frac{\partial k}{\partial x_j} \right) + G_k - \rho \varepsilon \quad (13)$$

$$\frac{\partial(\rho \varepsilon \bar{\mu}_i)}{\partial x_i} = \frac{\partial}{\partial x_j} \left(\alpha_\varepsilon \Psi_{\text{eff}} \frac{\partial \varepsilon}{\partial x_j} \right) + \frac{C_{1\varepsilon}^*}{k} G_k - C_{2\varepsilon} \rho \frac{\varepsilon^2}{k} \quad (14)$$

where:

$$\left. \begin{aligned} G_k &= \Psi_i S^2 \\ S &= \sqrt{2S_{ij}S_{ij}} \\ S_{ij} &= \frac{1}{2} \left(\frac{\partial \bar{\mu}_i}{\partial x_j} + \frac{\partial \bar{\mu}_j}{\partial x_i} \right) \\ \Psi_{\text{eff}} &= \Psi + \Psi_i, \Psi_i = \rho C_\Psi \frac{k^2}{\varepsilon} \\ C_\Psi &= 0.0845 \\ \alpha_k &= \alpha_\varepsilon = 1.39 \\ C_{1\varepsilon} &= 1.42 \\ C_{1\varepsilon}^* &= C_{1\varepsilon} - \frac{\vartheta(1 - \vartheta/\vartheta_0)}{1 + \gamma\vartheta^3} \\ \vartheta &= (2S_{ij} \cdot S_{ij})^{1/2} \frac{k}{\varepsilon} \\ \vartheta_0 &= 4.377, \gamma = 0.012, C_{2\varepsilon} = 1.68 \end{aligned} \right\} \quad (15)$$

2.4.3. Computational domain and simulation method

Turbine flow field was divided into inlet unit, turbine unit, and outlet unit, which were successively defined as Body-1, Body-2, and Body-3. Whole domain size is $\Phi 100 \text{ mm} \times 150 \text{ mm}$, the Body-1 is $\Phi 100 \text{ mm} \times 10 \text{ mm}$, the Body-2 is $\Phi 100 \text{ mm} \times 30 \text{ mm}$ (considering airfoil blade thickness is larger, so the airfoil turbine Body-2 is $\Phi 100 \text{ mm} \times 32 \text{ mm}$), the Body-3 is $\Phi 100 \text{ mm} \times 110 \text{ mm}$. The flow field structure is shown in Figs. 3a–c.

2.4.3.1. Generate mesh

Considering the influence of the number of grid nodes on the simulation results, we generated the flow field mesh by different numbers of mesh nodes (25×10^4 , 39×10^4 , 41×10^4 , 68×10^4 , 123×10^4 , 240×10^4 , and 321×10^4) and encrypted the surface of blade. The airfoil turbine head at 1,200 rpm was calculated, and the results showed that when the number of nodes reached 39×10^4 , the head were basically consistent, as shown in Fig. 4a. After comprehensive consideration of calculation accuracy and efficiency, the flow field with the number of nodes of 41×10^4 was selected.

In addition, y^+ was calculated to analyze the influence of the blade surface grid height on the calculated results. The airfoil turbine with the most complex structure was taken as the research object, and 40 points located on the upper and lower surface of the blade were calculated respectively, as shown in Fig. 4b. The value of y^+ was less than 50, which indicates the near-wall nodes were not within the laminar sub-layer [27]. Here, the blade boundary mesh was set to 0.2 mm. The flow field mesh is shown in Figs. 3d–f.

2.4.3.2. Set solver parameters

Three different time steps were set to calculate the static pressure of the turbine outlet section, and the results showed that the calculated results were consistent, as shown in Fig. 4c. After comprehensive consideration, set the time step to 1 second. Used the moving reference frame (MRF) method, and Body-2 was set as the rotation field [25,27]. The interface between different fluid domains was set by sliding mesh. The second-order implicit scheme was adopted for the turbulent simulation. SIMPLER algorithm was used to solve the pressure and velocity coupling at each time step [25,27].

The following two settings were used to study the flow field characteristics and backwashing efficiency.

- Boundary conditions of velocity-inlet and pressure-outlet were adopted, and the speed of Body-2 was set at 1,200 rpm.

Flow field characteristic was divided into distribution characteristic and energy characteristic. The distribution characteristic of the flow field was analyzed from two aspects of pressure and velocity. Pressure field distribution referred to the pressure change law of different sections along the direction of fluid movement in space, which reflected the interaction relationship between turbine and fluid. For ideal fluid, the decrease of pressure could directly reflect how much energy the fluid gains. In this study, blade surface, the inlet section, the outlet section, and two areas sections belonging to Body-3 were selected to establish the cloud diagram of pressure distribution. Based on the central plane of the turbine, an axial monitoring line parallel to the axis was established to analyze pressure changes along the monitoring line. Velocity field distribution referred to the law of velocity change in different sections along the direction of fluid movement. The original motion direction of fluid was changed due to the restriction of the channel when the fluid entered the turbine. The turbine continuously worked on the fluid, and the fluid presented a spiraling trajectory on the whole in space. In this paper, the cloud maps of axial velocity distribution were established by selecting sections at different locations. Based on the axial monitoring line, the distribution of axial tangential velocity was studied.

There was a large energy loss in the flow field, so it is inappropriate to simply use cascade efficiency to represent turbine efficiency. The loss caused by messy flows needed to be considered in the turbine, which was called vortex loss here. The relation between turbine cascade efficiency and vortex loss efficiency is shown in Eq. (16).

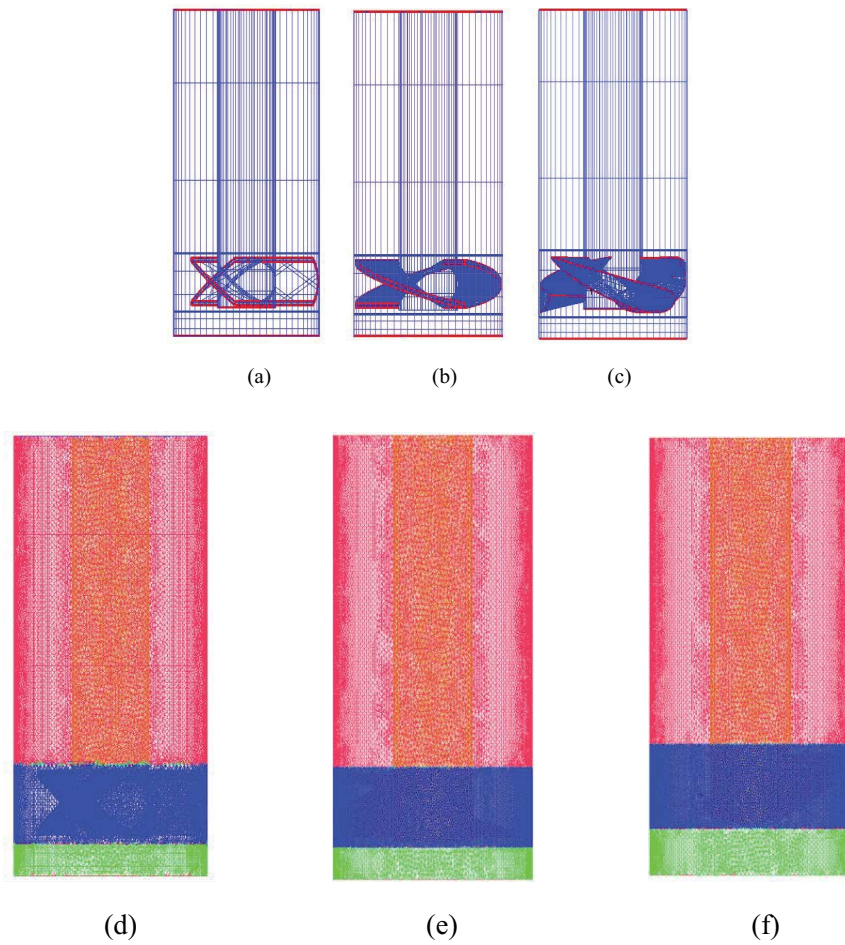


Fig. 3. (a–c) Flow field structure diagram, from left to right, flat turbine, bent plate turbine, and airfoil turbine and (d–f) flow field grid diagram, from left to right, flat turbine, bent plate turbine, and airfoil turbine.

Based on the simulation results, the total potential energy difference between the inlet and outlet of the turbine was represented as the head, and the $H-Q$ curve of various turbine speeds were calculated by using pump similarity law. The energy of the fluid flowing out of the turbine was taken as a useful work to calculate the hydraulic efficiency curve. In combination with cascade efficiency, Eq. (16) was used to solve vortex loss efficiency:

$$\eta = \eta_m \eta_h \tag{16}$$

$$\eta = \frac{P_{\text{axis}}}{P_{\text{useful}}} \tag{17}$$

- Boundary conditions of pressure-inlet and pressure-outlet were adopted, and the rotational speed was set at 600–2,000 rpm to simulate the working state of the internal circulation device.

According to the backwashing mechanism of the filter material, the velocity gradient, G value, was taken as the basis to measure the backwashing efficiency. In the axial dynamic backwashing device, the main effect on the filter

material was the strong washing-effect in the turbine, so only the energy consumption in the turbine was considered. The difference between the P_{axial} and the P_{useful} was obtained as the source of the G value. Based on simulated data and similarity law, the G value was calculated by Camp formula Eq. (18). The G values of all the filter materials in the filter tank and the filter materials in the turbine were calculated, respectively. The former was called macroscopic G value and the latter was called local G value. It was worth noting that the height of the internal circulation device was 0.5 m, and the minimum head required to form the internal circulation should be 0.5 m:

$$G = \sqrt{\frac{P}{\mu}} \tag{18}$$

2.5. Verification method

The experimental device used an airfoil turbine, and the head was expressed by measuring the height of the water column sucked by turbine. The suction heights of different rotational speeds were recorded, and the experimental results were compared with the simulation results.

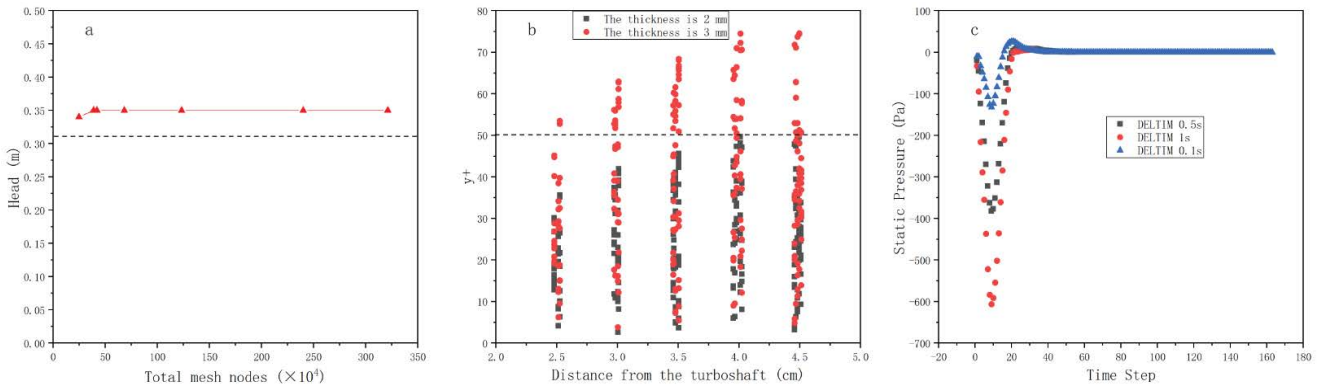


Fig. 4. Grid and time-step analysis diagram.

The accuracy of simulation results was verified by the head. The experimental process is shown in Fig. 5.

The walnut shell filter material with a diameter of 0.8–1.2 mm was loaded into the experimental device with a thickness of 0.05 m. The function of the filter material was to indicate the suction height after mixing with water when the turbine rotates. Filled the device with water. The water level was 0.3 m from the bottom of the device. The turbine speed was controlled by adjusting the frequency of the converter, and the height of the water column was recorded with a ruler. The relation between rotational speed and frequency is shown as Eq. (19):

$$n = \frac{60f}{b} \tag{19}$$

3. Results and discussion

3.1. Turbine cascade efficiency

According to Fig. 6, the cascade efficiency of the flat turbine increased slowly by 6% with the rising of the flow

rate, and then it was about 41%–47%. The cascade efficiency of the bent plate turbine basically remained unchanged, and was stable at about 41%. The cascade efficiency of the airfoil turbine was basically around 70%. The cascade efficiency of the three types turbine varied little with the rotational speed. The efficiency of plate turbine increased with the growing of flow rate, but the change range was small. It could be considered that the cascade efficiency of the three turbines has no significant associated with speed and flow rate. The cascade efficiency of flat blade turbine was slightly higher than bent plate turbine, and that of airfoil turbine was obviously higher than flat blade and bent plate. This indicated that the cascade efficiency of bent plate turbine compared with flat blade turbine decreases slightly due to the torsion characteristics, and the efficiency of airfoil turbine increases obviously due to the loading of airfoil.

3.2. Analysis of flow field distribution

According to Figs. 7a–c, contrast the pressure nephogram of the blade surface. The center of pressure of the

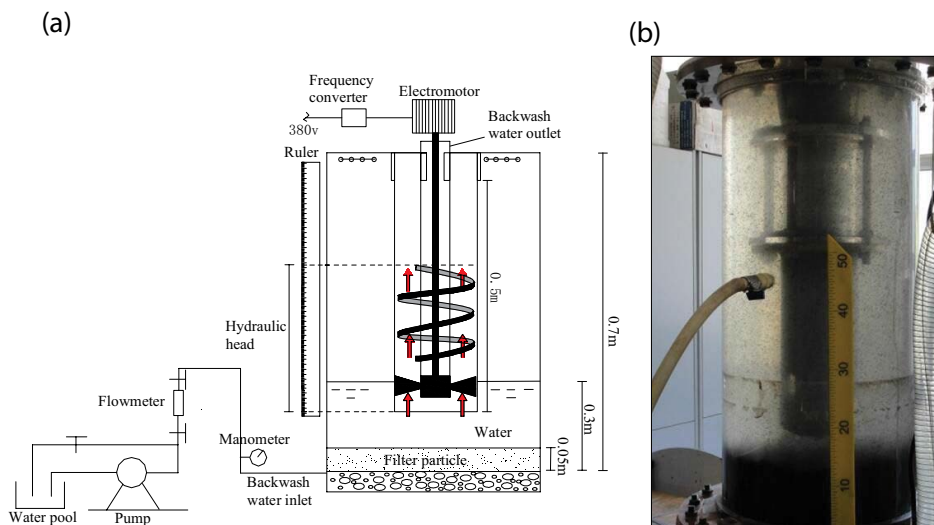


Fig. 5. Diagram of head verification experiment (the suction height of the turbine is measured with a ruler to characterize the turbine head): (a) schematic diagram and (b) device diagram.

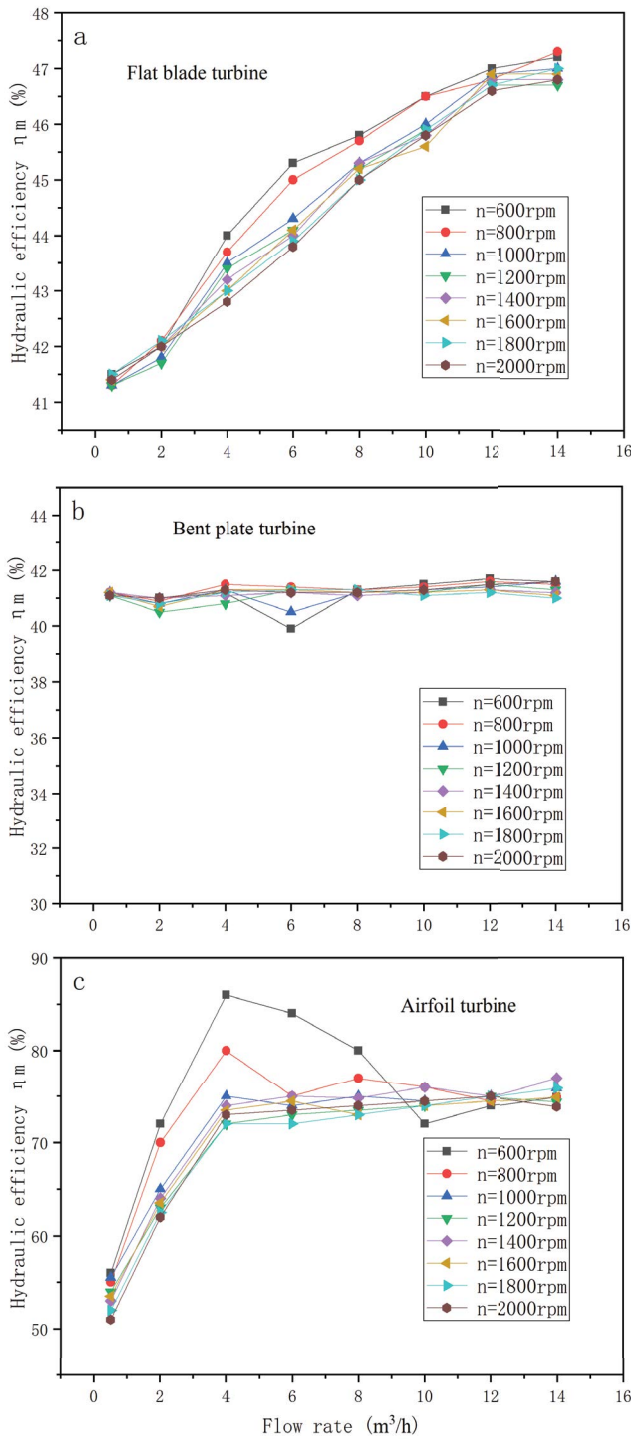


Fig. 6. Diagram of turbine cascade efficiency.

flat blade turbine was close to the outer edge of the turbine inlet, the pressure inlet side was higher than outlet side, and the pressure gradient was large. The pressure distribution center of the bent plate turbine and the airfoil turbine was basically at the geometric center of the blade, and the distribution was symmetrical in the center, with a small pressure gradient. Compared with the two twisted turbines, the pressure gradient on the surface of the flat turbine blade

was larger, and the fluid flow along the blade surface was more unstable. However, the pressure distribution of bent plate and airfoil turbine was similar because they have basically similar distortion characteristics. The twisted characteristic makes the difference.

According to Figs. 7d–f, contrast the pressure nephogram of the outlet section. Negative pressure and positive pressure existed in all three kinds of turbines, and the pressure gradient of the flat turbine was larger. The pressure distribution of the twisted turbine was similar. This indicated that the distortion characteristics lead to the outlet pressure distribution.

According to Figs. 7g–i, contrast flow field pressure nephogram. There was a larger pressure gradient at the inlet of the flat blade turbine. Except for the section of the turbine outlet, the pressure distributions of the three turbines were similar in the flow field. This indicated that the influence of flatness and twist on the pressure distribution of the flow field is more reflected in the inlet and outlet parts.

According to Fig. 8a, contrast the axial pressure profile. The pressure fluctuation at the inlet and outlet of the flat blade turbine was larger than the twisted turbine. The axial pressure change value of the flat turbine in the flow field was 4,000 Pa, and the twisted turbine was 6,000 Pa. This indicated that the flat blade turbine has larger energy loss, which mainly occurs at the inlet and outlet, and the twisted turbine has a better energy performance.

According to Figs. 7j–l, contrast the nephogram of axial velocity distribution in the flow field. All three types of turbines had different degrees of backflow. The reflux area of the outlet section was the largest in the flat blade turbine, and the two twisted turbines were similar. The large reflux area intuitively indicated that the flow field is turbulent and the energy loss will be large, so the twisted turbine has better performance for the two field structures.

According to Fig. 8b, contrast the distribution of axial tangential velocity profile. In the Body-3 section, the tangential velocity of the flat blade turbine fluctuated greatly around 1.5 m/s, and the tangential velocity at the outlet of the twisted turbine decreased steadily along the axial direction from 2 m/s. This was not consistent with the theory that the flat turbine agitates the fluid more violently and should give the fluid a greater tangential velocity. It was shown that the tangential velocity depends not only on the intensity of fluid agitation, but also on the energy loss.

According to Figs. 7m–o, the movement of fluid could directly reflect the flow field distribution and the interaction between the liquid flow and the blade. Particle activity could characterize the energy characteristics of the flow field. It was not difficult to see that the flat blade turbine had the most high-energy particles and low-energy particles, followed by the bent plate turbine and the least airfoil turbine. The flow at the inlet of the flat turbine was chaotic, which led to high pressure at the inlet of the flat blade and huge turbine energy loss.

3.3. Analysis of the vortex loss

According to Figs. 9a–c, the trend of turbine head was similar to that of axial flow pump, and the airfoil turbine head was the highest and the flat blade turbine was the

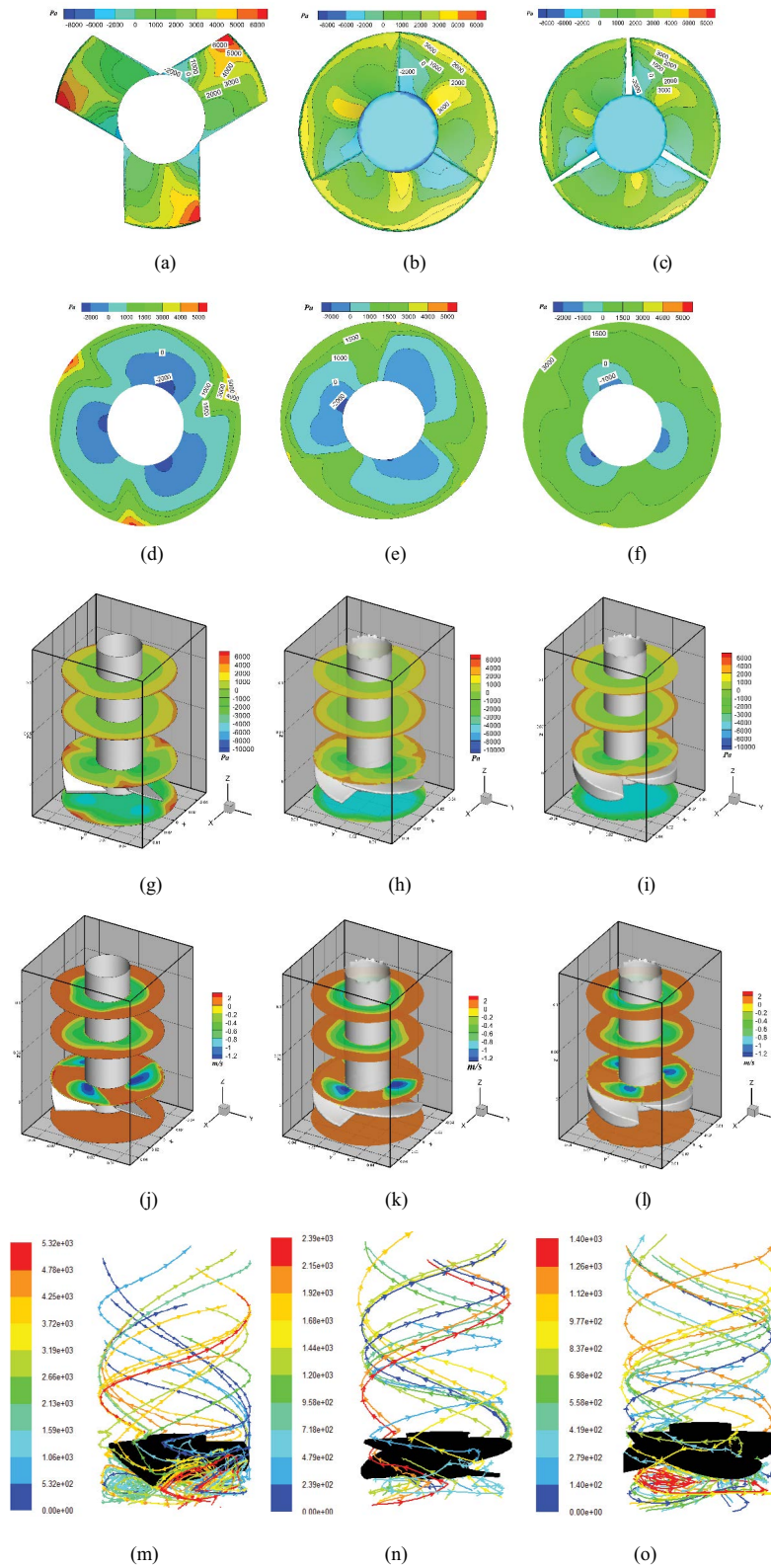


Fig. 7. (a–c) Pressure nephogram of blade surface, from left to right, flat blade turbine, bent plate turbine, and airfoil turbine, (d–f) the pressure nephogram of outlet section, from left to right, flat blade turbine, bent plate turbine, and airfoil turbine, (g–i) the pressure nephogram of flow field, from left to right, flat blade turbine, bent plate turbine, and airfoil turbine, (j–l) the axial velocity nephogram of flow field, from left to right, flat blade turbine, bent plate turbine, and airfoil turbine, and (m–o) particle activity trace, from left to right, flat blade turbine, bent plate turbine, and airfoil turbine.

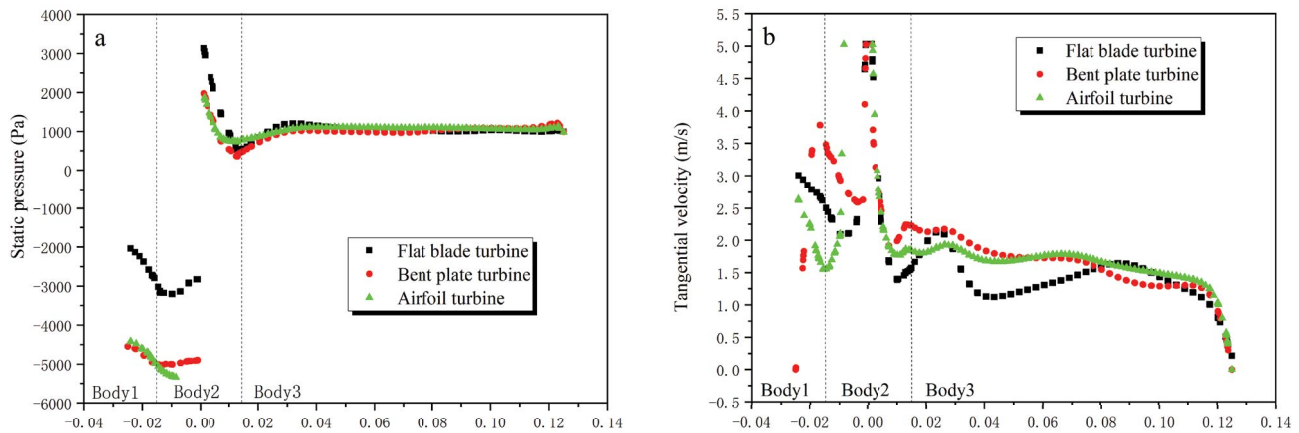


Fig. 8. (a) Pressure distribution of axial detection line and (b) pressure and tangential velocity distribution of axial detection line.

lowest. Looking at Fig. 9d, turbine hydraulic efficiency increased with the rising of rotating speed, among which airfoil turbine tended to 50%, bent plate turbine to 27.5%, and plate turbine to 10%. The efficiency of the airfoil turbine was significantly higher than the other two types of turbines. In addition, turbine efficiency differed greatly from cascade efficiency, indicating that vortex loss is an important factor affecting turbine efficiency.

According to Fig. 9e, the vortex loss efficiency increased with the rising of flow rate. When the flow was small, all three kinds of turbines produced strong turbulence, and the efficiency was very low. The flat turbine was always below 20%, indicating a large vortex loss and a strong irregular flow in the flow field. The efficiency of the two twisted turbines increased rapidly, reaching a maximum of 53.4%, indicating that the internal vortex loss gradually decreased and the flow gradually tended to be stable. At the same time, the efficiency laws of bent plate turbines and airfoil turbines were similar, which indicated that similar twisted characteristics lead to similar flow field distributions and thus lead to vortex losses.

3.4. Backwashing efficiency

- As shown in Fig. 10c, the minimum speeds required by flat blade turbine, bent plate turbine and airfoil turbine to achieved head of 0.5 m were 1,900; 1,720; and 1,420 rpm, respectively.
- The G value could reach 662 s^{-1} when air and water simultaneously backwashing [28]. According to Fig. 10d, the three types of turbines reached this value at 1,220; 1,515; and 1,730 rpm, respectively, and G value was 1,200; 720; and 450 when it just met head of 0.5 m. A larger G value could be generated by increasing the rotating speed. The flat blade turbine could reach twice G value of gas–water backwashing at 2,000 rpm.
- The above was the general calculation method of G value in the filter backwashing technology of particle filter at present, but for the axial dynamic backwashing, the actual washing process of the filter material in the turbine was ignored. The rubbing of the filter material were completed step by step, that was, the filter material entered the turbine in batches to complete cleaning

and regeneration. It was assumed that each filter material particle would fall back to the filter bed after being scrubbed only once, and 20% of the mixture involved in the rubbing was the filter material. According to Fig. 10e, the G value of the filter material inside the turbine was far greater than that of the gas–water backwashing, which could be up to 100 times. Compared with the macroscopic G value, the local G value had more reference significance. In addition, G value was not the bigger the better. Too large G value would aggravate the filter material wear. 50 times of the G value of gas–water backwashing was taken as the standard, which was reached for flat blade turbine, bent turbine and airfoil turbine at 1,290; 1,600; and 1,810 rpm, respectively.

- The local G value of the flat blade turbine and the bent plate turbine was too large at a rotation speed that met a head of 0.5 m. It not only aggravated the wear of filter material but also consumed more energy. Therefore, in a comprehensive consideration, the airfoil turbine was the most appropriate. The appropriate speed was 1,420–1,810 rpm, and the local G value was 35–45 times as big as the air and water backwashing.

3.5. Head verification

We carried out four times suction head tests, and different experimental results had some errors, mainly due to reading error caused by the movement of the walnut shell. According to Fig. 11, compared with the simulated value, the experimental values were always slightly smaller, and the relative difference between simulation and the measured head was about 12%. Since the density of walnut shells mixed with water increases, the suction height decreases. However, the difference is small, and by means of the linear fitting, the R^2 factor up to 0.99, showing a strong correlation between simulation and test, so the simulation is judged to be accurate.

4. Conclusions

- Based on the turbine mathematical model, the flat blade turbine endowed the fluid with greater circular velocity, and the twisted turbine endowed the fluid with more

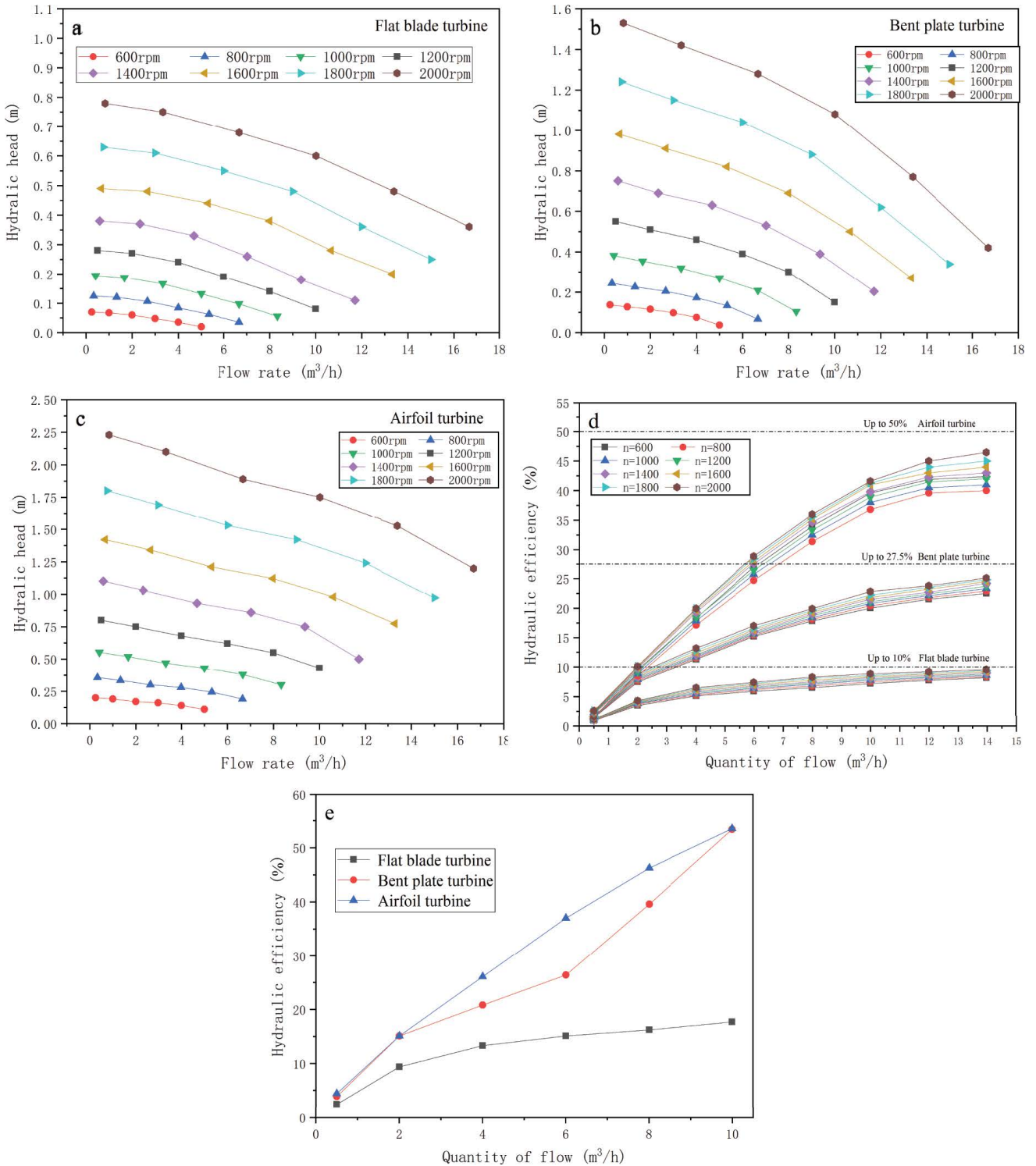


Fig. 9. (a–c) Flow-head diagram at multi-speed, (d) hydraulic efficiency diagram at multi-speed, and (e) efficiency diagram of vortex loss (1,200 rpm).

uniform circular velocity. Among the three types of turbines, the flow field in the flat blade turbine was the most uneven, and the flow of inlet and outlet were the most disorderly. The uniform distribution of circular velocity caused the twisted characteristic, and this distribution

was the reason for the relative stability of inlet and outlet flows.

- The cascades of both flat blade turbine and bent plate turbine were flat. They had similar cascade efficiency, and the twisted characteristic had no significant effect on the

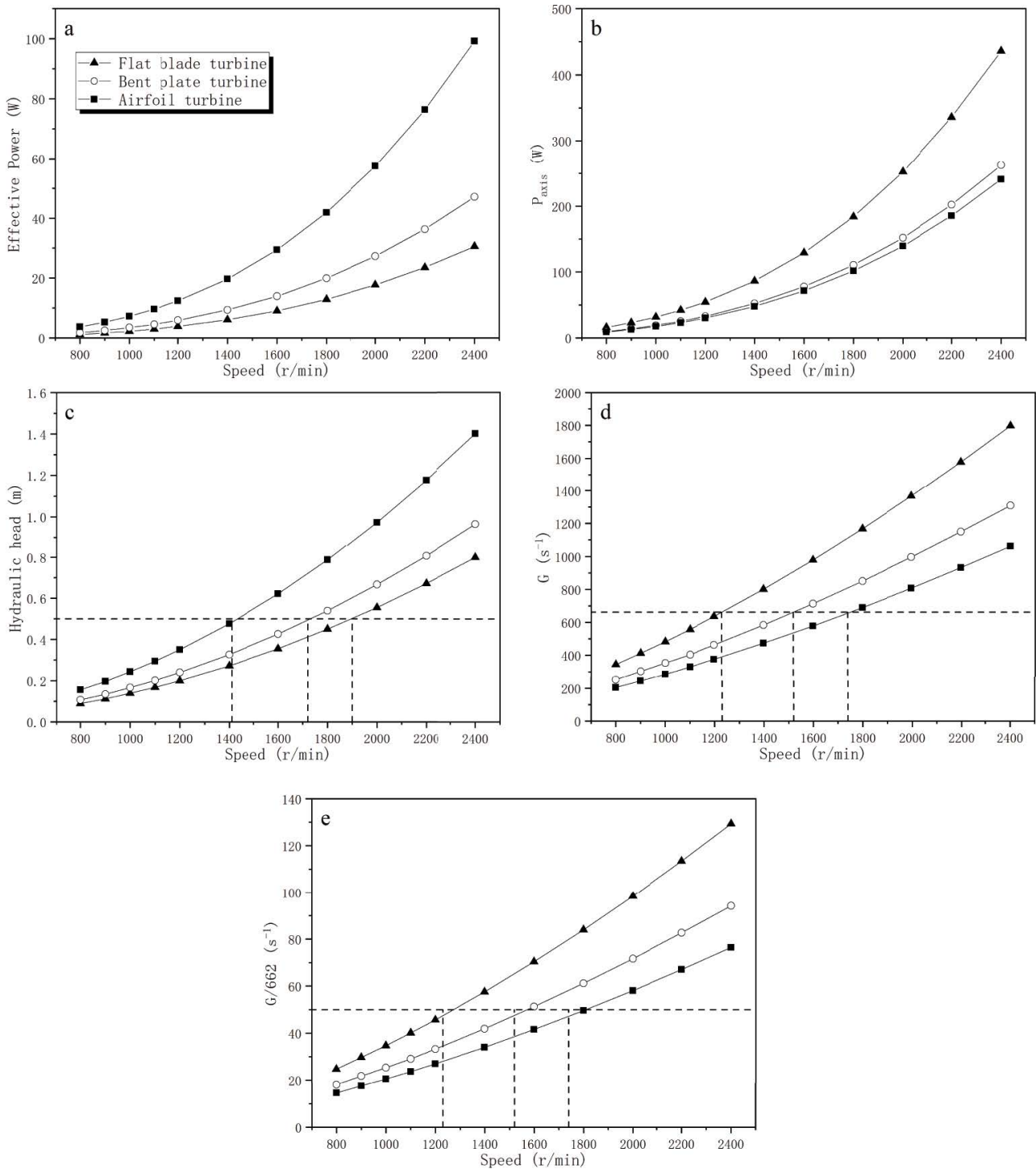


Fig. 10. (a) The effective work by the turbine at different speeds, (b) the axial work done by the turbine at different speeds, (c) the head diagram of the different rotational speed, and the minimum head of the turbine speed can be determined, (d) the macroscopic G value diagram, and (e) the local G value diagram of the turbine, the ratio of the local G value to the G value of the gas–water backwashing.

cascade efficiency. But the loading of the airfoil made the turbine cascade more efficient. On the other hand, the vortex loss efficiency of the two twisted turbines was similar, and the twisted characteristic was the main cause of vortex loss.

- Compared with gas–water backwashing, all three kinds of turbines could give a higher macroscopic G value to the fluid by adjusting the rotating speed. But the local G value had more reference value, compared with the macroscopic G value. The larger the G value was, the

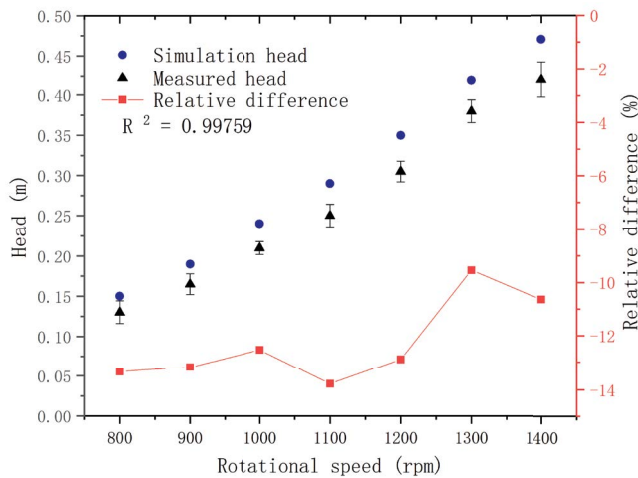


Fig. 11. Comparison of measured and simulation head for different rotation speeds. The error bars represent one unit of standard deviation.

more thorough the cleaning would be. Considering filter material wear and energy consumption, the optimal speed of the airfoil turbine was 1,420–1,810 rpm, and the local G value within this range was 35–45 times higher than the gas–water backwashing. Using axial turbines to backwashing had incomparable advantages such as high efficiency and controllability.

- Turbine backwashing efficiency was evaluated from the two aspects of minimum head and turbine efficiency. When the axial work was constant, the excessive efficiency led to a smaller G value, and the filter material could not obtain a good regeneration. Inversely, too small efficiency often could not satisfy the requirement of internal circulation. Therefore, turbine selection required comprehensive consideration.
- Using energy as a bridge, the relationship between three characteristics (flatness, twisted, and airfoil loading) and backwashing efficiency was established. The turbine with higher backwashing efficiency could be obtained by loading the airfoil and changing the degree of twisted. This opens the way for the development of technology and has a good prospect for development.

Acknowledgments

Supported by Beijing Natural Science Foundation (JQ19034), the National Key R&D Program of China (2018YFC0407403), National Natural Science Foundation of China (51722901), and Youth Innovation Talent Plan Project of Shihezi University (CXPY201902) are gratefully acknowledged.

Symbols

- β_1 and β_2 — Outlet angles of internal and external directrix respectively, and $\beta_1 = \beta_2$ (flat blade turbine), °
- r_1 and r_2 — Inside and the outside radius of the blade respectively ($r_1 < r_2$), cm
- ω — Rotational angular velocity, rad/s

- v_{u2} — Circumferential velocity of the turbine outlet with finite blades, m/s
- η_p — Efficiency of the infinitesimal cascade, %
- w_∞ — Relative velocity of the flow from infinity, m/s
- λ — Angle between the net force and lift, °
- v — Axial velocity of fluid near single cascade, m/s
- u — Relative velocity of fluid and cascade, m/s
- β_∞ — Angle between the incoming flow from infinity and the cascade axis, °
- η_h — Turbine cascade efficiency, %
- Q — Turbine flow, m³/h
- C_x — Drag coefficient
- C_y — Lift coefficient
- F_x — Pressure resistance, N
- F_y — Lift, N
- η_m — Vortex loss efficiency, %
- η — Turbine efficiency, %
- η_h — Turbine cascade efficiency, %
- P — Useful work, W
- $P_{\text{axis}}^{\text{useful}}$ — Axial work, W
- P — Power consumed by filter material per unit volume, W
- b — Frequency, Hz
- j — Number of pole-pairs of the motor, which is 1 here.
- \bar{p} — Average pressure
- $-\rho\mu'_i\mu'_j$ — Reynolds stress
- μ — Molecular viscosity
- ψ_t — Turbulent viscosity
- k — Turbulent kinetic energy

References

- [1] Y. Yang, X. Zhang, Z. Wang, Oilfield produced water treatment with surface-modified fiber ball media filtration, *Water Sci. Technol.*, 46 (2002) 165–170.
- [2] The Reinjection Standards (SY/15329–94), Chinese General Petroleum and Gas Incorporated, 1995.
- [3] C.Y. Li, L. Wei, Z.X. Chen, G. Yu, ASP flooding produced fluid characteristic and treatment process, *Adv. Energy Sci. Equip. Eng.*, (2015) 147–150.
- [4] B. Huang, J. Wang, W. Zhang, C. Fu, Y. Wang, X.B. Liu, Screening and optimization of demulsifiers and flocculants based on ASP flooding-produced water, *Processes*, 7 (2019) 239, doi: 10.3390/pr7040239.
- [5] L.H. Xu, Z.H. Tan, C.F. Zhang, Y.H. Liu, C. Li, X.Z. Zhang, J.P. Wu, Q.L. Xie, Performance and microbial diversity of a full-scale oilfield wastewater treatment plant, *Desal. Water Treat.*, 99 (2017) 239–247.
- [6] H. Sun, X. He, Q. Tang, X.B. Li, Recyclable polyetherpolyquaternium grafted SiO₂ microsphere for efficient treatment of ASP flooding-produced water: oil adsorption characteristics and mechanism, *RSC Adv.*, 10 (2020) 15124–15131.
- [7] F.B.P.D.S. Almeida, K.P.S.O.R. Esquerre, J.I. Soletti, C.E.D. Silva, Coalescence process to treat produced water: an updated overview and environmental outlook, *Environ. Sci. Pollut. Res.*, 26 (2019) 28668–28688.
- [8] S.B. Deng, R.B. Bai, J.P. Chen, G. Yu, Z.P. Jiang, F.S. Zhou, Effects of alkaline/ surfactant/polymer on stability of oil droplets in produced water from ASP flooding, *Colloids Surf., A*, 211 (2002) 275–284.
- [9] H. Sun, Q.Q. Wang, X.B. Li, X. He, Novel polyetherpolyquaternium copolymer as an effective reverse demulsifier for O/W emulsions: demulsification performance and mechanism, *Fuel*, 263 (2020) 116770, doi: 10.1016/j.fuel.2019.116770.

- [10] A.Y. Liu, S.Y. Liu, Study on performance of three backwashing modes of filtration media for oilfield wastewater filter, *Desal. Water Treat.*, 57 (2016) 10498–10505.
- [11] C.S.B. Fitzpatrick, Observations of particle detachment during filter backwashing, *Water Sci. Technol.*, 27 (1993) 213–221.
- [12] F.Y. Zhang, A.X. Jiang, L. Zhang, B. Yan, F. Li, The backwashing mechanism and efficiency of low pressure and steady flow walnut shell filter, *Water Wastewater Eng.*, 33 (2007) 89–93 (in Chinese with English abstract).
- [13] Q.Y. Liu, Y. Dai, Y. Luo, Y.L. Chen, Ultrasonic-intensified chemical cleaning of nano filtration membranes in oilfield sewage purification systems, *J. Eng. Fibers Fabr.*, 11 (2016) 17–25.
- [14] P. Chen, Z.X. Chen, C.Y. Bai, Technology current situation and understanding of the treatment process of produced water in Daqing oilfield, *Oil Gas Field Surf. Eng.*, 37 (2018) 19–24 (in Chinese with English abstract).
- [15] S. Wang, Z.C. Yu, H. Wu, Axial Dynamic Backwashing Filter, CN201832460U, 2011.
- [16] S. Wang, Z.C. Yu, H. Wu, The Backwashing Method and Device of the Filter, CN101982216A, 2011.
- [17] X.G. Dong, Z.C. Yu, S.M. Liu, Z.G. Wang, B. Sun, Z. Wei, Y.M. Wang, Research on the filtration efficiency and backwashing characteristics of axial dynamic rubber/diamond sand filter bed process, *Ind. Water Treat.*, 37 (2017) 25–28 (in Chinese with English abstract).
- [18] Z.C. Yu, Y.L. Niu, X.G. Dong, S.M. Liu, B.J. Zhao, B. Sun, X.Y. Liu, C. Sun, Experiment on binary wastewater filtration by axial dynamic backwashing method, *Oil Gas Field Surf. Eng.*, 34 (2015) 15–17+21 (in Chinese with English abstract).
- [19] Z.C. Yu, Y.L. Niu, Z. Li, S. Wang, F. Li, H.Y. Lin, H.M. Cui, Effect of polymer concentration on filtration and backwashing process by the axial dynamic backwashing method, *Chemistry*, 78 (2015) 733–737 (in Chinese with English abstract).
- [20] X.G. Dong, S.M. Liu, Z.C. Yu, B. Sun, Y.L. Niu, Experimental study on the filtration of wastewater containing polymer by axial dynamic backwashing filter, *Ind. Water Treat.*, 35 (2015) 86–89 (in Chinese with English abstract).
- [21] Z.C. Yu, D.X. Wang, Z.G. Wang, S. Wang, Y.M. Wang, Determination of theoretical time of axial dynamic backwashing method for deep bed filtration in oilfield, *Fresenius Environ. Bull.*, 27 (2018) 6876–6883.
- [22] Y. Mao, M.X. Shi, Guide vane design and calculation of axial flow cyclone, *J. China Univ. Pet.*, 3 (1983) 306–318 (in Chinese with English abstract).
- [23] D.L. He, X.H. Shi, S.Z. Song, The 3D modeling method of lamina of axial flow impeller based on Solidworks, *Mach. Des. Manuf.*, 6 (2005) 51–52 (in Chinese with English abstract).
- [24] J. Yan, The influence of limited blades of runner on outlet flow, *Sichuan Univ. Sci. Technol.*, 3 (1992) 201–205 (in Chinese with English abstract).
- [25] D.S. Zhang, W.D. Shi, B. Chen, X.F. Guan, Unsteady flow analysis and experimental investigation of axial-flow pump, *J. Hydrodyn.*, 22 (2010) 35–43.
- [26] F.J. Wang, Y.J. Li, G.H. Cong, W.E. Wang, H.X. Wang, CFD simulation of 3D flow in large-bore axial-flow pump with half-elbow suction sump, *J. Hydrodyn.*, 18 (2006) 243–247.
- [27] Y.J. Li, F.J. Wang, Numerical investigation of performance of an axial-flow pump with inducer, *J. Hydrodyn.*, 19 (2007) 705–711.
- [28] G.B. Li, J.X. Liu, T.L. Zheng, Mechanism analysis on filter air scour and water backwashing, *J. Harbin Inst. Archit. Eng.*, 2 (1992) 56–61 (in Chinese with English abstract).